JOEMS

Journal of Opto-Electro-Medic Science

Vol. 1, No. 2, June 2025, pp. 27-32, DOI: 10.59190/joems.v1i2.301

PUBLISHED BY LSPRAR

Factors contributing to slice loss in small-angle X-ray scattering tensor tomography in real space: A review

Yuri Situmorang

Department of Physics, Universitas Riau, Pekanbaru 28293, Indonesia

ABSTRACT

X-ray small-angle scattering tensor tomography (SAXSTT) technique is an innovative method that enables 3D tomographic reconstruction of large-volume voxels non-destructively. This study identifies factors that affect slice loss in SAXSTT in real space. Results show that the quality and resolution of the resulting images are strongly influenced by the signal to noise ratio, absorption, as well as scattering in the sample. In addition, parameters such as collimator and slice thickness during CT scanning prove crucial for obtaining optimal image results. Reconstruction using SAXSTT shows great potential in high-precision material analysis, especially in applications where sample integrity is required to be maintained.

ARTICLE INFO

Article history:

Received Apr 11, 2025
Revised May 14, 2025
Accepted Jun 18, 2025

Keywords:

3D Reconstruction
SAXSTT
Scattering
Tensor Tomography
X-Ray

* **Corresponding Author**
E-mail address: yuri.situmorang3030@student.unri.ac.id

1. INTRODUCTION

Small-angle scattering tensor tomography is an innovative approach capable of tomographically reconstructing three-dimensional reciprocal spaces from large-volume voxels. Small-angle scattering tensor tomography can enhance the principle of X-ray computed tomography, which typically reconstructs tensors on a per-voxel basis. The mean dots per voxel for the complete sample of over 10,000 voxels was 0.84, while for the six slices exhibiting fewer truncation clipping artefacts, the dot product rose to 0.91 [1].

A novel method for obtaining localised two-dimensional small-angle X-ray scattering signals involves utilising an optical X-ray phase modulator composed of a circular grating array. Omnidirectional scattering can be obtained for each pixel of the image by assessing the alteration in the circular lines prior to and subsequent to the insertion of the sample into the beam path. Measurements of local two-dimensional small-angle X-ray scattering signals are conducted at various angular orientations of the sample relative to the input beam. The sensitivity of all-directional scattering on a circular grating significantly reduces the measurement time required to acquire the local small-angle X-ray scattering signal, in contrast to other experimental techniques. Upon reconstructing the local two-dimensional small-angle X-ray scattering signal, the scattering tensor delineates characteristic [2].

X-rays facilitate the acquisition of information regarding the interior structure of materials in a non-destructive manner. In conventional X-ray imaging, like in numerous other modalities, a trade-off between spatial resolution and field of view (FOV) is unavoidable. The effective detector pixel size is several micrometres, and with thousands of detector pixels, the field of view is constrained to a few millimetres. The small-angle X-ray scattering signal manifests as the Fourier transform of the spatially unresolved fine structure electron density autocorrelation function [3].

The application of Monte Carlo methods in radiation dosimetry is experiencing exponential growth. Owing to their extensive application, computer simulation techniques are increasingly favoured for reference dosimetry calculations and treatment planning. The current availability of computational capacity facilitates 3D shape simulation utilised in clinical accelerator treatment heads, ionisation chambers, and other detectors, as well as patient treatment using data and Computed Tomography [4].

2. THEORITICAL REVIEW

2.1. X-rays

X-rays are a form of electromagnetic energy, akin to visible light or radio waves, that capture X-ray scattering patterns at minimal angles. The spatial resolution is dictated by the beam size and the dimensions of the scanning step. It is typically selected within the range of several micrometres to several tens of micrometres, although it can also be as little as several tens of nanometres or as large as a few millimetres [5].

2.2. Small Angle Scattering Tensor Tomography (SASTT)

Small-angle scattering tensor tomography is an innovative approach utilised for the tomographic reconstruction of three-dimensional reciprocal spaces from large-volume voxels. Small-angle scattering tensor tomography can enhance the principle of X-ray computed tomography, which typically reconstructs tensors on a per-voxel basis. The mean dots per voxel for the comprehensive sample of over 10,000 voxels is 0.84, whereas for six slices exhibiting fewer truncation clipping artefacts, the dot product rises to 0.91 [1, 6, 7].

2.3. Tomographic Sections

The term tomography is derived from the Greek word tomos, signifying to cut, divide, or overlay. Computed tomography use sophisticated computer algorithms to obtain data and transform it into cross-sectional layers or "slices" of the human anatomy. Computed tomography use computerised techniques to analyse data acquired from the passage of X-rays through anatomical regions. X-rays are composed of energy packets known as photons. Photons infiltrate or are dispersed by the anatomical structures of the body [8-10].

2.4. Nanostructures

Nanostructures are assemblies of bound atoms with dimensions spanning from 1 to 100 nm in one dimension, predominantly comprising atoms engaged in interfacial environments and interactions among the constituent domains. Single-phase nanostructures, including nanocrystals, nanotubes, nanorods, or nanowires composed of specific materials [11]. Nanostructures exhibit diverse sizes, forms, and structures, originating from multiple sources. Nanostructures may exhibit conical, helical, spherical, flat hollow, tubular, cylindrical, or irregular forms. Carbon-based nanostructures are composed of carbon compounds. Diamond nanocrystals manifest as allotropic carbon with a cubic crystal structure composed of interconnected units [12].

3. MATERIALS AND METHOD

3.1. Tomographic Technique

Industrial process tomography systems utilise measurement concepts such as nuclear electronic, optical, acoustic, microwave, NMR, and electrical approaches.

3.2. Photon Transmission Tomography

The premise of transmission tomography involves measuring the intensity of radiation that traverses an item and is detected by a set of sensors. The source and detector arrays revolve around the object. The magnitude refers to the intensity of radiation traversing an object and being detected by a network of sensors. The attenuation of a photon beam is governed by Beer's Law:

$$1 - \varepsilon = \frac{1}{\int \mu(s) ds} \ln \frac{I_0}{I} \tag{1}$$

where, $1 - \varepsilon$ is average concentration, μ is linear absorption coefficient, s is photon beam trajectory; I and I_0 are observed gearbox values with and without materials in the pipe.

3.3. Gamma Ray Tomography

γ-ray tomography developed from the initial industrial usage of γ-densitometry, which employed a radiation source and detector to assess the average density along a photon beam trajectory.

3.4. X-ray Tomography

Unlike γ-rays, where photons are produced by the spontaneous disintegration of atomic nuclei, photons in X-ray tomography are generated within an X-ray tube. The electrons are accelerated by a substantial electric voltage between the heated cathode and anode.

A CT scan is an imaging technique that generates three-dimensional images from two-dimensional X-ray data. The X-ray tube operates by rotating around the patient, whose movement resembles that of a ring. The detector receives the transmitted light, converts the analogue data into digital format, and the computer processes the image. CT scans possess exceptionally high resolution, featuring slices that are 0.1 to 0.2 mm in thickness. This layer employs X-rays with extremely short wavelengths, resulting in images that are clearer than those produced by ultrasonography (CT scans can generate images of bones, lungs, brain, and vascular structures in a single examination).

3.5. Electrical Capacitance Tomography

Electrical capacitance tomography (ECT) is a method that utilises variations in capacitance to rebuild the internal configuration of an item. In fluidised beds, it can be confidently asserted that measuring only the capacitive component of impedance is enough, given that the process medium lacks electrical conductivity [13, 14].

3.6. Scanning Methodologies

The material chosen for this study was trabecular bone that was fixed and embedded in polymethyl methacrylate (PMMA). A cube was removed from the mass and subsequently machined into a cylinder with a diameter and height of 1.2 mm using a bespoke lathe equipment. The X-ray energy was established at 12.4 keV utilising a Si (111) dual crystal monochromator, and the scattering pattern was captured on a Pilatus 2M detector positioned at a sample-to-detector distance of 2. A flight tube, approximately 2 meters in length, was positioned between the sample and the detector to mitigate air scattering. A 1.5 mm steel beam stopper within the fly tube obstructs the transmitted beam directly. The fluorescence signal from the beam stop is directly proportional to the intensity. The magnitude of the X-rays impacting was quantified using a Cyberstar (Oxford Danfysik). This enables the measurement of the relative X-ray transmission through the sample. The sample is assessed using a beam having a full width at half maximum of 12 mm to 24 mm, as determined by knife edge scanning. The raster scan employs a step size of 25 mm in both vertical and horizontal orientations, accompanied by continuous fly scanning in the vertical axis. Figure 1(a) depicts the experimental setup. Two sets of small angle X-ray scattering tensor tomography measurements were conducted, each comprising 224 scanning SAXS pictures.

In the initial set of SAXSTT measurements, the base of the cylindrical sample was affixed to the PMMA needle tip with water-soluble hot glue (Norland Blocking Adhesive 107). Prior to the second SAXSTT experiment, the sample was affixed using UV adhesive (Norland Optical Adhesive 81) to the second pin, subsequent to which the first pin was removed by immersing the sample in hot water. The second pin was positioned at an angle of approximately 90 degrees relative to the first pin, measured around the directional axis of the a total of 1,716,960 scattering pictures were recorded. The initial data set measurement lasted 1218 minutes, whereas the subsequent data set measurement lasted 1364 minutes.

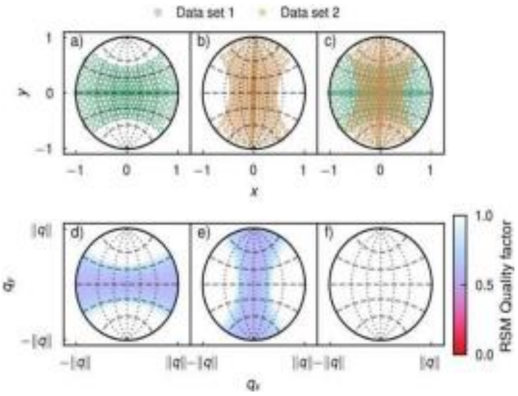

Figures 1. Illustrate the quality factor F of the hemisphere in reciprocal space. The spots on the projection hemisphere and the theoretical quality factor: (a) the spots evaluated on the projection sphere during the initial measurement; (b) the points evaluated in the second measurement; (c) the aggregate points of the two measures; (d) quality factor in reciprocal space of the initial dataset; (e) quality factor of the secondary data set; and (f) quality factor of the aggregated data collection. The dashed line denotes the great circle at longitudes 0°, 30°, and 60°, with the y-axis serving as the meridian. The dotted line indicates the little circle at longitudes 0°, 30°, and 60°, with the x-axis representing the equator.

3.7. Measurement Angle (Coverage)

The quality factor exhibits the anticipated symmetry, with measurements across the entire great semicircle resulting in a quality factor of 1 at places perpendicular to this semicircle. The minimum quality factor achieved is 0.5, corresponding to the least coverage (for a data set of 1) of the great semicircle, which occurs when the semicircle is positioned along a single longitude and varies solely in latitude. The semicircle remains encompassed by measurements at a fixed longitude and latitude (slope, for dataset 1) over the range [45°, 45°]; hence, in the most worst scenario, half of the complete semicircle arc length of 180° is encompassed. A q range of 0.597-0.607 nm was employed for reconstruction and analysis, corresponding to a d-spacing range of 10.36-10.53 nm. This range was utilised due to artefacts in the second test at the lower q range, potentially caused by water-soluble glue infiltrating the outer layer during installation.

4. RESULTS AND DISCUSSIONS

4.1. Comparative Analysis of Complete and Partial Data Reconstruction

Valid voxels for comparison, specifically those containing trabecular bone samples, were determined based on the average amplitude of each RSM in the reconstruction of the complete data set. The position of each marker in Figures 2 (a) and 2 (b) aligns with the mode of the RSM basis function, while the colour of the marker represents the error derived from comparing the coefficients of that basis function with the corresponding coefficients from the complete dataset reconstruction.

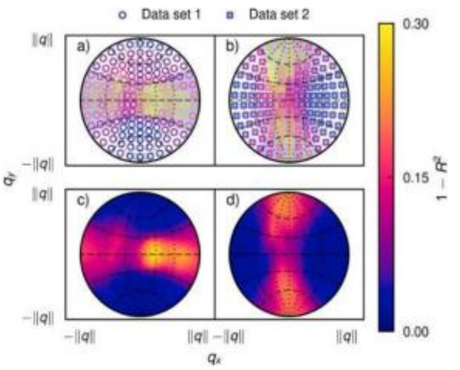

Figure 2. Error allocation for each RSM basis function: (a) coefficient error for dataset 1; (b) coefficient error for dataset 2; (c) RSM error for dataset 1; (d) RSM mistake for dataset 2.

The mark is overlayed on the quality factor of the reciprocating space. Figures 2 (c) and 2 (d) illustrate the error in amplitude at each location on the reciprocating spatial sphere. The error distribution in the amplitude of the reciprocating space adheres precisely to the quality factor, with errors exceeding approximately 0.1 occurring solely in areas where the quality factor is less than 1. The errors in the basis set coefficients depicted in Figures 2 (a) and 2 (b) exceed the amplitude errors shown in Figures 2 (c) and 2 (d), a discrepancy that is especially evident when contrasting the upper section of Figure 2 (a) with the corresponding section in Figure 2 (c). This is elucidated by the overlapping nature of the basis set functions, which are not orthogonal. This indicates that certain fluctuations in the basis set coefficients negate one another during the assessment of each RSM function's amplitude for error computation.

4.2. Impact of Reconstruction Error on Nanostructure Assessment

The mean amplitude is a significant scalar quantity utilised for q-resolved reconstruction and subsequent analysis of the nanostructural information included in the SAXS curve. The relative anisotropy is remarkably consistent across all three reconstructions, exhibiting negligible deviations. A more pronounced disparity is observable in the fibre symmetry factor. The comprehensive dataset exhibits a high concentration at the centre of the interface, but the partial dataset appears to have a diminished factor along the peripheries. Consequently, the fibre symmetry factor exhibits more sensitivity to absent slices compared to the conventional relative anisotropy. The supplementary texture in the equatorial scattering ring manifests as an absent slice artefact. One of the most significant attributes obtainable from SAXSTT measurements is the local orientation; thus, it is crucial to examine the extent of uncertainty introduced by the missing wedge problem in its determination.

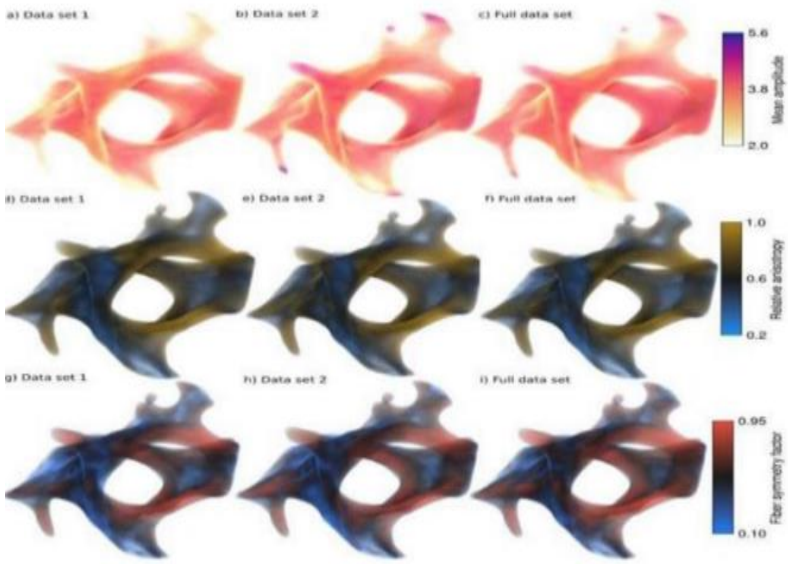

Figure 3. Volume rendering of scalar variables: panels (a) – (c) illustrate the mean amplitude of the RSM for partial data sets 1 and 2, in addition to the comprehensive data set; panels (d) – (f) illustrate the relative anisotropy of the RSM; and panels (g) – (i) illustrate the RSM fibre symmetry factor.

The highlighted region depicted in green and orange rectangles signifies an area within the trabecular bone where domains of varying orientations overlap. This region exhibits the most significant orientation inaccuracy in both partial datasets. In comparison to Figures 3 (a) to 2 (i), it is evident that the most significant orientation errors are seen in areas characterised by low relative anisotropy and symmetry of the fibres. This indicates that the orientation is poorly defined and may encompass numerous orientations within a voxel. This aligns with areas featuring domain interfaces with varying orientations. A like tendency is observed in the overall RSM error, which closely resembles the distribution of orientation error [15].

4. CONCLUSION

The X-ray small-angle scattering tensor tomography technique can augment or recreate 3D tomography from large-volume voxels. This method facilitates the non-destructive examination of material properties and structures, rendering it an invaluable asset in material research. The quality and resolution of the resultant images are considerably affected by elements including the signal-to-noise ratio, absorption, and scattering inside the sample. To attain optimal imaging outcomes, it is crucial to consider characteristics such as the collimator and slice thickness during CT scanning. This method offers significant promise for high-precision material analysis while preserving the integrity of the sample.

REFERENCES

[1] Guizar-Sicairos, M., Georgiadis, M., & Liebi, M. (2020). Validation study of small-angle X-ray scattering tensor tomography. *Synchrotron Radiation*, **27**(3), 779–787.

[2] Auenhammer, R. M., Kim, J., Oddy, C., Mikkelsen, L. P., Marone, F., Stampanoni, M., & Asp, L. E. (2024). X-ray scattering tensor tomography based finite element modelling of heterogeneous materials. *npj Computational Materials*, **10**(1), 50.

[3] Kim, J., Kagias, M., Marone, F., Shi, Z., & Stampanoni, M. (2021). Fast acquisition protocol for X-ray scattering tensor tomography. *Scientific Reports*, **11**(1), 23046.

[4] Andreo, P. (2018). Monte Carlo simulations in radiotherapy dosimetry. *Radiation Oncology*, **13**, 1–15.

[5] Liebi, M., Georgiadis, M., Kohlbrecher, J., Holler, M., Raabe, J., Usov, I., Menzel, A., Schneider, P., Bunk, O., & Guizar-Sicairos, M. (2018). Small-angle X-ray scattering tensor tomography: Model of the three-dimensional reciprocal-space map, reconstruction algorithm and angular sampling requirements. *Foundations of Crystallography*, **74**(1), 12–24.

[6] Nielsen, L. C., Erhart, P., Guizar-Sicairos, M., & Liebi, M. (2023). Small-angle scattering tensor tomography algorithm for robust reconstruction of complex textures. *Foundations of Crystallography*, **79**(6), 515–526.

[7] Wollweber, T. & Ayyer, K. (2024). Nanoscale x-ray imaging with high spectral sensitivity using fluorescence intensity correlations. *Structural Dynamics*, **11**(2).

[8] Fatimah, S., binti Ismail, N. F., Masrochah, S., Dartini, S. K. M., Darmini, S. S., Aryani, A. I., & binti Ali, A. (2024). *Pencitraan diagnostik wanita: Prinsip, patologi umum dan modalitas imejing*. Cendikia Mulia Mandiri.

[9] Soeprijanto, B. (2017). *Imejing diagnostik pada anomali kongenital sistem traktus urinarius*. Airlangga University Press.

[10] Blykers, B. K., Organista, C., Boone, M. N., Kagias, M., Marone, F., Stampanoni, M., ... & Aelterman, J. (2021). Tunable X-ray dark-field imaging for sub-resolution feature size quantification in porous media. *Scientific Reports*, **11**(1), 18446.

[11] Meyers, R. (2001). *Physical science and technology*. USA: Academic Press.

[12] Koduru, J. R., Karri, R. R., & Mubarak, N. M. (2023). *Hybrid nanomaterials for sustainable applications: Case studies and applications*. Elsevier.

[13] Abd Rashid, W. N., Mohamad, E. J., Abdul Rahim, R., Abdullah, J., & Mohmad Ameran, H. L. (2016). Electrical capacitance tomography: A review on portable ECT system and hardware design. *Sensor Review*, **36**(1), 64–70.

[14] Dyakawski, T. & Jaworski, J. (2001). *Handbook of conveying and handling of particular*. Amsterdam: Elsevier.

[15] Nielsen, L. C., Tänzer, T., Rodriguez-Fernandez, I., Erhart, P., & Liebi, M. (2024). Investigating the missing-wedge problem in small-angle X-ray scattering tensor tomography across real and reciprocal space. *Synchrotron Radiation*, **31**(5).